KSME

Springer

Journal of Mechanical Science and Technology 38 (4) 2024

Original Article
DOI 10.1007/s12206-024-0307-6

Keywords:
· High-speed train
· Lateral running stability
· Anti-yaw damper
· Model predictive control
· Disturbance observer

Correspondence to:
Ruqiang Mou
scumrq2013@163.com;
Chunjun Chen
cjchen@swjtu.edu.cn

Citation:
Mou, R., Chen, C., Chen, C., Zhang, Y. (2024). Analysis and control of high-speed train lateral vibration on the basis of a conditionally triggered model predictive control strategy. Journal of Mechanical Science and Technology 38 (4) (2024) 1703~1717.
http://doi.org/10.1007/s12206-024-0307-6

Received October 23rd, 2023
Revised January 1st, 2024
Accepted January 15th, 2024

† Recommended by Editor
No-cheol Park

Analysis and control of high-speed train lateral vibration on the basis of a conditionally triggered model predictive control strategy

Ruqiang Mou[1,2], Chunjun Chen[1,3], Chaoyue Chen[1] and Yaowen Zhang[1]

[1]School of Mechanical Engineering, Southwest Jiaotong University, Chengdu 610031, China, [2]Department of Automation Engineering, The Engineering & Technical College, Chengdu University of Technology, Leshan 614000, China, [3]Technology and Equipment of Rail Transit Operation and Maintenance Key Laboratory of Sichuan Province, Southwest Jiaotong University, Chengdu 610031, China

Abstract The lateral vibration of the car body affects the lateral stability of high-speed trains (HSTs), and the aim of this study is to design a good control strategy to decrease the lateral vibration of the car body. First, the Maxwell model of the anti-yaw damper was transformed into a Voigt model by the equivalence method, and a modified 17-degree-of-freedom (DOF) lateral vibration model that includes the anti-yaw damper was established. After the design difficulty and control accuracy of the control strategy were weighed, the lateral and yaw motions of the wheelsets were regarded as disturbances, and a disturbance observer of wheelset motions was designed to simplify the 17-DOF model to a 9-DOF lateral vibration model. Second, a model predictive control (MPC) strategy for HST lateral vibration was designed, and the effects of the key parameters on the lateral vibration acceleration of the HST car body and on the iterative computation time of the MPC strategy were studied. In addition, a conditionally triggered model predictive control (CMPC) strategy was proposed. Last, the control effects of the CMPC strategy under the working conditions of speed change, turnout passage, and aerodynamic load were studied by simulation, which verified the validity of the proposed model and control strategy.

1. Introduction

The maximum running speed of the Chinese Fuxing EMU at present is 350 km/h. During the 14th Five-Year Plan period, China is expected to vigorously develop its CR450 high-speed train (HST) with a speed of 400 km/h to improve transportation efficiency. However, increasing the running speed reduces the stability and safety of HSTs, especially when HSTs pass through turnouts or meet inside and outside of tunnels. In addition, the vibration of the HST car body is transmitted to the passengers through the seats, and passengers are sensitive to lateral vibration. Therefore, studying the lateral vibration control strategy is important to improve the comfort of passengers and the lateral stability of the HST car body.

To the best of the authors' knowledge, the main HST lateral vibration models available have 17, 7, and 3 degrees of freedom (DOFs). The classical 17-DOF lateral vibration model [1–3] includes car body lateral, yaw, and roll motions; bogie lateral, yaw, and roll motions; and wheelset lateral and yaw motions, but it does not consider the anti-yaw damper. Existing HSTs in China are equipped with anti-yaw dampers, so this model needs to be modified. Meanwhile, the 3-DOF lateral vibration model that includes car body and bogie lateral motions was established to design second-order sliding mode [4] and repetitive learning controllers [5]. This model reduces the difficulty of control strategy design but ignores the body and bogie yaw motions, so it is considerably different from the HST physical model. In addition, the control effect is difficult to guarantee in practical application. The 7-DOF lateral vibration model [6, 7] that includes car

body lateral, yaw, and roll motions and bogie lateral and yaw motions is close to the HST physical model, but the model's accuracy decreases when the HST passes through a curved track with a large-amplitude roll motion. Therefore, a novel HST lateral vibration model that considers the design difficulty and control accuracy of the control strategy needs to be established.

Many control strategies [8] have been proposed for HST lateral vibration. The skyhook damping control strategy [9] can improve HST lateral running stability in low-frequency ranges but cannot do so in high-frequency ranges. The skyhook-acceleration damping control strategy [10, 11] can improve HST lateral running stability over a large frequency range, but it cannot easily calculate the precise crossover frequency in practical application. In addition, the skyhook and displacement–velocity control strategy [12] can suppress the lateral vibration of the HST car body to ensure the safety and lateral stability of the HST, but it also needs to calculate the precise crossover frequency. By contrast, the skyhook–groundhook hybrid damping control strategy [13] realizes balance between the lateral vibrations of the car body and bogie. The balance coefficient can be adjusted by fuzzy control, but effective fuzzy control rules are difficult to design. The bio-inspired chaotic fruit and fuzzy logic hybrid control strategy [14] can marginally improve the HST running safety index when the HST moves on straight lines or curves. In addition, the linear–quadratic–Gaussian (LQG) control strategy [15, 16] suppresses car body lateral vibration by solving the optimal control gain, so it has an obvious control effect and is suitable for situations with fixed operating conditions. However, actual operating conditions vary with time, so the adaptability of LQG is poor. PID, PID + skyhook damping, and linear–quadratic control strategies [17] can improve HST ride quality. In addition, the sliding mode control strategy [4] can considerably decrease the lateral vibration acceleration of the HST car body, but it cannot eliminate the chattering problem. The repetitive learning control strategy [5] can reduce the lateral vibration acceleration of the car body and has the advantages of dynamic optimization and adaptability. However, the adopted vibration model is too simple, and its practical application effect is affected.

The generalized predictive control method based on controller matching for HSTs can track the speed and displacement well [18]. The iterative learning control method based on predictive control for HSTs solves the problem of difficult-to-adjust PID parameters, improves system robustness, and has good speed tracking ability [19]. In addition, the hierarchical model predictive control (MPC) strategy [20, 21] minimizes HST delays and cancellations through online delay management and HST speed control. The adaptive MPC method [22] that combines the estimated parameter adaptive updating law and MPC can effectively address the time-varying problem of the HST drag coefficient and can make the HST accurately track the desired speed under the final bounded tracking error. Compared with other control strategies, MPC has the advantages of high control accuracy and robustness. Extensive research has been conducted on HST velocity tracking control, but minimal research has been performed on HST lateral vibration control. Therefore, the MPC strategy is used to decrease the HST lateral vibration in this study. However, standard MPC requires extensive computational effort and long iterative computation time. To address these challenges, researchers [23–26] have proposed the self-triggered MPC strategy, which inspired us to design the conditionally-triggered model predictive control (CMPC) strategy of HST lateral vibration.

The main contributions of this study can be summarized as follows:

1) A method of transforming the Maxwell model into a Voigt model was provided, and a modified 17-DOF lateral vibration model that includes the anti-yaw damper was established to improve the accuracy of the HST lateral vibration model.

2) The lateral and yaw motions of the HST wheelsets were regarded as disturbances, and a disturbance observer (DOB) was designed to estimate wheelset motions. The DOB effectively simplified the model and reduced the difficulty of control strategy design.

3) A novel CMPC strategy that realizes matching control of the lateral vibration, computational effort, and iterative computation time of HST was established.

2. Model and problem formulation

2.1 Model design

2.1.1 Anti-yaw damper model

The physical model, Maxwell model, and Voigt model of the anti-yaw damper are shown in Fig. 1. The Maxwell model is consistent with the physical model, but its forces are difficult to calculate. By contrast, the Voigt model is simple, and its forces are easy to calculate, so it is suitable for control strategy design. After the accuracy of the anti-yaw damper model and the design difficulty of the control strategy are weighed, the Maxwell model is converted to the Voigt model by using the equivalence method [27]. The conversion process is as follows.

Assuming that $x = A\sin(\omega t)$, the Maxwell model mechanical equilibrium equation is expressed as follows:

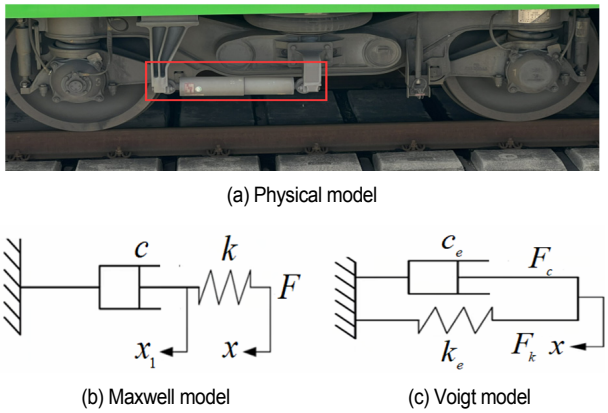

(a) Physical model

(b) Maxwell model

(c) Voigt model

Fig. 1. Anti-yaw damper.

$$k(x_1 - x) + c\dot{x}_1 = 0 . \tag{1}$$

The expression of x_1 is obtained by Laplace transform as follows:

$$x_1 = \frac{Ak^2}{k^2 + c^2\omega^2}\sin(\omega t) - \frac{Akc\omega}{k^2 + c^2\omega^2}\cos(\omega t) , \tag{2}$$

where ω is the excitation frequency, which is consistent with the track irregularity excitation frequency acting on the HST wheelsets. Although the track irregularity excitation frequency changes, the main vibration frequency is the one that exerts a considerable influence on the lateral vibration of the HST car body. Thus, this study set ω as the main vibration frequency of the HST car body lateral vibration. Then, force was obtained as follows:

$$F = c\dot{x}_1 = \frac{Ak^2c\omega}{k^2 + c^2\omega^2}\cos(\omega t) + \frac{Akc^2\omega^2}{k^2 + c^2\omega^2}\sin(\omega t) . \tag{3}$$

The forces for the Voigt model can be obtained from Eq. (3).

$$F_k = \frac{kc^2\omega^2}{k^2 + c^2\omega^2}A\sin(\omega t) \tag{4}$$

$$F_c = \frac{k^2c}{k^2 + c^2\omega^2}A\omega\cos(\omega t) . \tag{5}$$

In accordance with system frequency characteristic theory, the equivalent stiffness (k_e) and equivalent damping (c_e) of the Voigt model were obtained as follows:

$$k_e = \frac{kc^2\omega^2}{k^2 + c^2\omega^2} , \tag{6}$$

$$c_e = \frac{k^2c}{k^2 + c^2\omega^2} . \tag{7}$$

In this study, we used the abovementioned method to convert the Maxwell model into a Voigt model for anti-yaw damper modeling.

2.1.2 HST lateral vibration model

As shown in Fig. 2, the HST model is composed of the car body, the bogie, wheelsets, primary suspension, secondary suspension, and the anti-yaw damper. Compared with the classical 17-DOF HST lateral vibration model, the improved model includes the anti-yaw damper. The model inputs, outputs, and control forces and their symbols are shown in Table 1.

In accordance with Newton's second law, the dynamic equations of HST lateral vibration were established as follows.

1) Dynamic equation of car body lateral motion

$$\begin{aligned} M_c\ddot{y}_c = &-4K_{sy}y_c + 4K_{sy}h_{cs}\phi_c + 2K_{sy}y_{t1} + 2K_{sy}h_{ts}\phi_{t1} + 2K_{sy}y_{t2} \\ &+ 2K_{sy}h_{ts}\phi_{t2} - 4C_{sy}\dot{y}_c + 4C_{sy}h_{cs}\dot{\phi}_c + 2C_{sy}\dot{y}_{t1} + 2C_{sy}h_{ts}\dot{\phi}_{t1} \\ &+ 2C_{sy}\dot{y}_{t2} + 2C_{sy}h_{ts}\dot{\phi}_{t2} - 4K_{sdy}y_c + 4K_{sdy}h_{csl}\phi_c \\ &- 2K_{sdy}l_{csl1}\psi_c + 2K_{sdy}l_{csl2}\psi_c + 2K_{sdy}y_{t1} + 2K_{sdy}y_{t2} \\ &+ 2K_{sdy}h_{tsl}\phi_{t1} + 2K_{sdy}h_{tsl}\phi_{t2} - 4C_{sdy}\dot{y}_c + 4C_{sdy}h_{csl}\dot{\phi}_c \\ &- 2C_{sdy}l_{csl1}\dot{\psi}_c + 2C_{sdy}l_{csl2}\dot{\psi}_c + 2C_{sdy}\dot{y}_{t1} + 2C_{sdy}\dot{y}_{t2} \\ &+ 2C_{sdy}h_{tsl}\dot{\phi}_{t1} + 2C_{sdy}h_{tsl}\dot{\phi}_{t2} + 2K_{ls}y_c - 2K_{ls}h_{cls}\phi_c \\ &- K_{ls}y_{t1} - K_{ls}h_{tls}\phi_{t1} - K_{ls}y_{t2} - K_{ls}h_{tls}\phi_{t2} \\ &- F_{l1} - F_{r1} - F_{l2} - F_{r2} \end{aligned} \tag{8}$$

Table 1. Model inputs, outputs, and control forces and their symbols ($i = 1, 2$, $j = 1; i = 3, 4$, $j = 2$).

	Symbol	Description
Inputs	y_a	Lateral alignment of track irregularity
	θ_e	Cross level of track irregularity
Outputs	y_c, ϕ_c, ψ_c	Lateral displacement, roll angle, and yaw angle of the car body
	$y_{tj}, \phi_{tj}, \psi_{tj}$	Lateral displacement, roll angle, and yaw angle of the bogie
	y_{wi}, ψ_{wi}	Lateral displacement and yaw angle of the wheelsets
Control forces	F_{l1}, F_{r1}	Lateral control force at the left and right sides of the front car body
	F_{l2}, F_{r2}	Lateral control force at the left and right sides of the rear car body

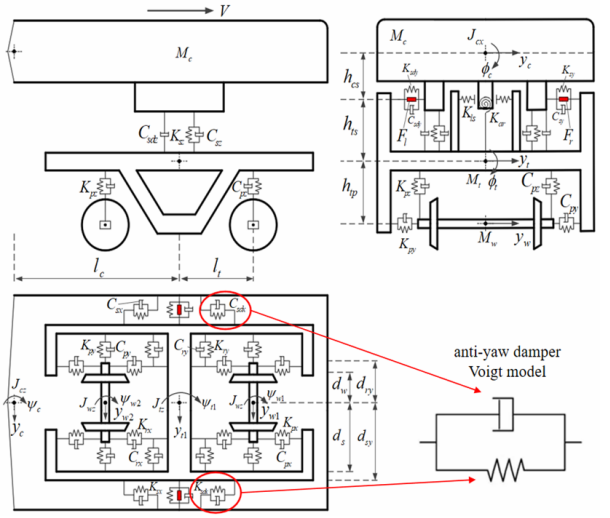

Fig. 2. Simplified spatial geometry model of HST.

2) Dynamic equation of car body roll motion

$$\begin{aligned} J_{cx}\ddot{\phi}_c = &4K_{sy}h_{cs}y_c - 4K_{sy}h_{cs}^2\phi_c - 2K_{sy}h_{cs}y_{t1} - 2K_{sy}h_{ts}h_{cs}\phi_{t1} \\ &- 2K_{sy}h_{ts}h_{cs}\phi_{t2} + 4C_{sy}h_{cs}\dot{y}_c - 4C_{sy}h_{cs}^2\dot{\phi}_c - 2C_{sy}h_{cs}\dot{y}_{t1} \\ &- 2C_{sy}h_{ts}h_{cs}\dot{\phi}_{t1} - 2C_{sy}h_{cs}\dot{y}_{t2} - 2C_{sy}h_{ts}h_{cs}\dot{\phi}_{t2} + 4K_{sdy}h_{csl}y_c \\ &- 4K_{sdy}h_{csl}h_{csl}\phi_c + 2K_{sdy}l_{csl1}h_{csl}\psi_c - 2K_{sdy}l_{csl2}h_{csl}\psi_c \\ &- 2K_{sdy}h_{csl}y_{t1} - 2K_{sdy}h_{csl}y_{t2} - 2K_{sdy}h_{tsl}h_{csl}\phi_{t1} \\ &- 2K_{sdy}h_{tsl}h_{csl}\phi_{t2} + 4C_{sdy}h_{csl}\dot{y}_c - 4C_{sdy}h_{csl}h_{csl}\dot{\phi}_c \end{aligned}$$

$$
\begin{aligned}
&+2C_{sdy}l_{csl1}h_{csl}\dot{\psi}_c-2C_{sdy}l_{csl2}h_{csl}\dot{\psi}_c-2C_{sdy}h_{csl}\dot{y}_{t1}\\
&-2C_{sdy}h_{tsl}h_{csl}\dot{\phi}_{t1}-2C_{sdy}h_{tsl}h_{csl}\dot{\phi}_{t2}-2K_{ls}h_{cls}y_c\\
&+2K_{ls}h_{cls}h_{cls}\phi_c+K_{ls}h_{cls}y_{t1}+K_{ls}h_{tls}h_{cls}\phi_{t1}+K_{ls}h_{cls}y_{t2}\\
&+K_{ls}h_{tls}h_{cls}\phi_{t2}-4K_{sz}d_s^2\phi_c+2K_{sz}d_s^2\phi_{t1}+2K_{sz}d_s^2\phi_{t2}\\
&-4C_{sz}d_s^2\dot{\phi}_c+2C_{sz}d_s^2\dot{\phi}_{t1}+2C_{sz}d_s^2\dot{\phi}_{t2}-4C_{sdz}d_{sv}^2\dot{\phi}_c\\
&+2C_{sdz}d_{sv}^2\dot{\phi}_{t1}+2C_{sdz}d_{sv}^2\dot{\phi}_{t2}-2K_{ar}\phi_c+K_{ar}\phi_{t1}+K_{ar}\phi_{t2}\\
&+(F_{l1}+F_{r1}+F_{l2}+F_{r2})h_{csl}
\end{aligned}
\tag{9}
$$

3) Dynamic equation of car body yaw motion

$$
\begin{aligned}
J_{cz}\ddot{\psi}_c=&-4K_{sy}l_cl_c\psi_c+2K_{sy}l_cy_{t1}+2K_{sy}l_ch_{ts}\phi_{t1}-2K_{sy}l_cy_{t2}\\
&-2K_{sy}l_ch_{ts}\phi_{t2}-4C_{sy}l_cl_c\dot{\psi}_c+2C_{sy}l_c\dot{y}_{t1}+2C_{sy}l_ch_{ts}\dot{\phi}_{t1}\\
&-2C_{sy}l_c\dot{y}_{t2}-2C_{sy}l_ch_{ts}\dot{\phi}_{t2}-K_{sdy}(l_{csl1}+l_{csl2})^2\psi_c\\
&+K_{sdy}(l_{csl1}+l_{csl2})y_{t1}+K_{sdy}(l_{csl1}+l_{csl2})h_{tsl}\phi_{t1}\\
&+K_{sdy}(l_{csl1}-l_{csl2})l_{tsl}\psi_{t1}-K_{sdy}(l_{csl1}+l_{csl2})y_{t2}\\
&-K_{sdy}(l_{csl1}+l_{csl2})h_{tsl}\phi_{t2}+K_{sdy}(l_{csl1}-l_{csl2})l_{tsl}\psi_{t2}\\
&-C_{sdy}(l_{csl1}+l_{csl2})^2\dot{\psi}_c+C_{sdy}(l_{csl1}+l_{csl2})\dot{y}_{t1}\\
&+C_{sdy}(l_{csl1}+l_{csl2})h_{tsl}\dot{\phi}_{t1}+C_{sdy}(l_{csl1}-l_{csl2})l_{tsl}\dot{\psi}_{t1}\\
&-C_{sdy}(l_{csl1}+l_{csl2})\dot{y}_{t2}-C_{sdy}(l_{csl1}+l_{csl2})h_{tsl}\dot{\phi}_{t2}\\
&+C_{sdy}(l_{csl1}-l_{csl2})l_{tsl}\dot{\psi}_{t2}-K_{ls}l_cy_{t1}-K_{ls}l_ch_{tls}\phi_{t1}\\
&+K_{ls}l_cy_{t2}+K_{ls}l_ch_{tls}\phi_{t2}-4K_{sx}d_sd_s\psi_c+2K_{sx}d_sd_s\psi_{t1}\\
&+2K_{sx}d_sd_s\psi_{t2}-4C_{sx}d_sd_s\dot{\psi}_c+2C_{sx}d_sd_s\dot{\psi}_{t1}\\
&+2C_{sx}d_sd_s\dot{\psi}_{t2}-4K_{sdx}d_{sy}\psi_c+2K_{sdx}d_{sy}\psi_{t1}\\
&+2K_{sdx}d_{sy}\psi_{t2}-4C_{sdx}d_{sy}\dot{\psi}_c+2C_{sdx}d_{sy}\dot{\psi}_{t1}\\
&+2C_{sdx}d_{sy}\dot{\psi}_{t2}-(F_{l1}+F_{r1}-F_{l2}-F_{r2})l_c
\end{aligned}
\tag{10}
$$

4) Dynamic equation of bogie lateral motion

$$
\begin{aligned}
M_t\ddot{y}_{tj}=&-4K_{py}y_{tj}-4K_{py}h_{tp}\phi_{tj}-4C_{py}\dot{y}_{tj}-4C_{py}h_{tp}\dot{\phi}_{tj}\\
&+2K_{py}y_{wj}+2K_{py}y_{w(2j)}+2C_{py}\dot{y}_{wj}+2C_{py}\dot{y}_{w(2j)}\\
&-4K_{ry}y_{wj}+4K_{ry}h_{tr}\phi_{tj}-4C_{ry}\dot{y}_{tj}+4C_{ry}h_{tr}\dot{\phi}_{tj}\\
&+2K_{ry}y_{wj}+2K_{ry}y_{w(2j)}+2C_{ry}\dot{y}_{wj}+2C_{ry}\dot{y}_{w(2j)}\\
&+2K_{sy}y_c-2K_{sy}h_{cs}\phi_c-2(-1)^jK_{sy}l_c\psi_c-2K_{sy}y_{tj}\\
&-2K_{sy}h_{ts}\phi_{tj}+2C_{sy}\dot{y}_c-2C_{sy}h_{cs}\dot{\phi}_c-2(-1)^jC_{sy}l_c\dot{\psi}_c\\
&-2C_{sy}\dot{y}_{tj}-2C_{sy}h_{ts}\dot{\phi}_{tj}+2K_{sdy}y_c-2K_{sdy}h_{csl}\phi_c\\
&-2(-1)^jK_{sdy}l_{cslj}\psi_c-2K_{sdy}y_{tj}-2K_{sdy}h_{tsl}\phi_{tj}\\
&+2C_{sdy}\dot{y}_c-2C_{sdy}h_{csl}\dot{\phi}_c-2(-1)^jC_{sdy}l_{cslj}\dot{\psi}_c\\
&-2C_{sdy}\dot{y}_{tj}-2C_{sdy}h_{tsl}\dot{\phi}_{tj}-K_{ls}y_c+K_{ls}h_{cls}\phi_c\\
&+(-1)^jK_{ls}l_c\psi_c+K_{ls}y_{tj}+K_{ls}h_{tls}\phi_{tj}+F_{lj}+F_{rj}
\end{aligned}
\tag{11}
$$

5) Dynamic equation of bogie roll motion

$$
\begin{aligned}
J_{tx}\ddot{\phi}_{t1}=&-4K_{py}h_{tp}y_{tj}-4K_{py}h_{tp}h_{tp}\phi_{tj}-4C_{py}h_{tp}\dot{y}_{tj}-4C_{py}h_{tp}h_{tp}\dot{\phi}_{tj}\\
&+2K_{py}h_{tp}y_{wj}+2K_{py}h_{tp}y_{w(2j)}+2C_{py}h_{tp}\dot{y}_{wj}+2C_{py}h_{tp}\dot{y}_{w(2j)}\\
&+4K_{ry}h_{tr}y_{tj}-4K_{ry}h_{tr}h_{tr}\phi_{tj}+4C_{ry}h_{tr}\dot{y}_{tj}-4C_{ry}h_{tr}h_{tr}\dot{\phi}_{tj}\\
&-2K_{ry}h_{tr}y_{wj}-2K_{ry}h_{tr}y_{w(2j)}-2C_{ry}h_{tr}\dot{y}_{wj}-2C_{ry}h_{tr}\dot{y}_{w(2j)}\\
&-4K_{pz}d_wd_w\phi_{tj}-4C_{pz}d_wd_w\dot{\phi}_{tj}-4C_{pdz}d_{pv}d_{pv}\dot{\phi}_{tj}+2K_{sy}h_{ts}y_c\\
&-2K_{sy}h_{ts}h_{cs}\phi_c-2(-1)^jK_{sy}h_{ts}l_c\psi_c-2K_{sy}h_{ts}y_{tj}-2K_{sy}h_{ts}h_{ts}\phi_{tj}\\
&+2C_{sy}h_{ts}\dot{y}_c-2C_{sy}h_{ts}h_{cs}\dot{\phi}_c-2(-1)^jC_{sy}h_{ts}l_c\dot{\psi}_c-2C_{sy}h_{ts}\dot{y}_{tj}\\
&-2C_{sy}h_{ts}h_{ts}\dot{\phi}_{tj}2K_{sdy}h_{tsl}y_c-2K_{sdy}h_{tsl}h_{csl}\phi_c\\
&-2(-1)^jK_{sdy}h_{tsl}l_{cslj}\psi_c-2K_{sdy}h_{tsl}y_{tj}-2K_{sdy}h_{tsl}h_{tsl}\phi_{tj}\\
&+2C_{sdy}h_{tsl}\dot{y}_c-2C_{sdy}h_{tsl}h_{csl}\dot{\phi}_c-2(-1)^jC_{sdy}h_{tsl}l_{cslj}\dot{\psi}_c\\
&-2C_{sdy}h_{tsl}\dot{y}_{tj}-2C_{sdy}h_{tsl}h_{tsl}\dot{\phi}_{tj}+2K_{sz}d_sd_s\phi_c-2K_{sz}d_sd_s\phi_{tj}\\
&+2C_{sz}d_sd_s\dot{\phi}_c-2C_{sz}d_sd_s\dot{\phi}_{tj}+2C_{sdz}d_{sv}d_{sv}\dot{\phi}_c-2C_{sdz}d_{sv}d_{sv}\dot{\phi}_{tj}\\
&-K_{ls}h_{tls}y_c+K_{ls}h_{cls}h_{tls}\phi_c+(-1)^jK_{ls}l_ch_{tls}\psi_c+K_{ls}h_{tls}y_{tj}\\
&+K_{ls}h_{tls}h_{tls}\phi_{tj}+K_{ar}\phi_c-K_{ar}\phi_{tj}+(F_{lj}+F_{rj})h_{tsl}
\end{aligned}
\tag{12}
$$

6) Dynamic equation of bogie yaw motion

$$
\begin{aligned}
J_{tz}\ddot{\psi}_{tj}=&-4K_{py}l_tl_t\psi_{tj}-4C_{py}l_tl_t\dot{\psi}_{tj}+2K_{py}l_ty_{wj}-2K_{py}l_ty_{w(2j)}\\
&+2C_{py}l_t\dot{y}_{wj}-2C_{py}l_t\dot{y}_{w(2j)}-4K_{ry}l_{tr}l_{tr}\psi_{tj}-4C_{ry}l_{tr}l_{tr}\dot{\psi}_{tj}\\
&+2K_{ry}l_{tr}y_{wj}-2K_{ry}l_{tr}y_{w(2j)}+2C_{ry}l_{tr}\dot{y}_{wj}-2C_{ry}l_{tr}\dot{y}_{w(2j)}\\
&-4K_{px}d_wd_w\psi_{tj}-4C_{px}d_wd_w\dot{\psi}_{tj}+2K_{px}d_wd_w\psi_{wj}\\
&+2K_{px}d_wd_w\psi_{w(2j)}+2C_{px}d_wd_w\dot{\psi}_{wj}+2C_{px}d_wd_w\dot{\psi}_{w(2j)}\\
&-4K_{rx}d_{ry}d_{ry}\psi_{tj}-4C_{rx}d_{ry}d_{ry}\dot{\psi}_{tj}+2K_{rx}d_{ry}d_{ry}\psi_{wj}\\
&+2K_{rx}d_{ry}d_{ry}\psi_{w(2j)}+2C_{rx}d_{ry}d_{ry}\dot{\psi}_{wj}+2C_{rx}d_{ry}d_{ry}\dot{\psi}_{w(2j)}\\
&+2K_{sx}d_sd_s\psi_c-2K_{sx}d_sd_s\psi_{tj}+2C_{sx}d_sd_s\dot{\psi}_c-2C_{sx}d_sd_s\dot{\psi}_{tj}\\
&+2K_{sdx}d_{sy}d_{sy}\psi_c-2K_{sdx}d_{sy}d_{sy}\psi_{tj}+2C_{sdx}d_{sy}d_{sy}\dot{\psi}_c\\
&-2C_{sdx}d_{sy}d_{sy}\dot{\psi}_{tj}-2K_{sdy}l_{tsl}l_{tsl}\psi_{tj}-2C_{sdy}l_{tsl}l_{tsl}\dot{\psi}_{tj}
\end{aligned}
\tag{13}
$$

7) Dynamic equation of wheelset lateral motion

$$
\begin{aligned}
M_w\ddot{y}_{wi}=&(2K_{py}+2K_{ry})y_{tj}+(2K_{py}h_{tp}-2K_{ry}h_{tr})\phi_{tj}\\
&-(-1)^j(2K_{py}l_t+2K_{ry}l_{tr})\psi_{tj}-(2K_{py}+2K_{ry}+K_{gy})y_{wi}\\
&+2f_{22}\psi_{wi}+(2C_{py}+2C_{ry})\dot{y}_{tj}+(2C_{py}h_{tp}-2C_{ry}h_{tr})\dot{\phi}_{tj}\\
&-(-1)^j(2C_{py}l_t+2C_{ry}l_{tr})\dot{\psi}_{tj}-(2C_{py}+2C_{ry}+\frac{2f_{22}}{V})\dot{y}_{wi}\\
&+K_{gy}(y_{ai}+r_o\theta_{ci})
\end{aligned}
\tag{14}
$$

8) Dynamic equation of wheelset yaw motion

$$
\begin{aligned}
J_{wz}\ddot{\psi}_{wi}=&2K_{px}d_wd_w\psi_{tj}+2C_{px}d_wd_w\dot{\psi}_{tj}-2K_{px}d_wd_w\psi_{wi}\\
&-2C_{px}d_wd_w\dot{\psi}_{wi}+2K_{rx}d_{ry}d_{ry}\psi_{tj}+2C_{rx}d_{ry}d_{ry}\dot{\psi}_{tj}\\
&-2K_{rx}d_{ry}d_{ry}\psi_{wi}-2C_{rx}d_{ry}d_{ry}\dot{\psi}_{wi}+2(-1)^iK_{ry}l_{wr}y_{tj}\\
&-2(-1)^iK_{ry}l_{wr}h_{tr}\phi_{tj}-2K_{ry}l_{wr}l_{tr}\psi_{tj}-2(-1)^iK_{ry}l_{wr}y_{wi}\\
&+2(-1)^iC_{ry}l_{wr}\dot{y}_{tj}-2(-1)^iC_{ry}l_{wr}h_{tr}\dot{\phi}_{tj}-2C_{ry}l_{wr}l_{tr}\dot{\psi}_{tj}\\
&-2(-1)^iC_{ry}l_{wr}\dot{y}_{wi}-\frac{2f_{11}b\lambda}{r_o}y_{wi}-\frac{2f_{11}bb}{V}\dot{\psi}_{wi}\\
&+\frac{2f_{11}b\lambda}{r_o}(y_{ai}+r_o\theta_{ci})+K_{g\psi}\psi_{wi}
\end{aligned}
\tag{15}
$$

2.1.3 Track irregularity model

The lateral alignment and cross level of track irregularity are the main factors that cause lateral vibration of the HST car body. The German low-interference track spectrum and the Chinese high-speed railway ballastless track spectrum are commonly used track irregularity spectrum for HST speeds above 250 km/h. From the viewpoint of track spectrum amplitude and wavelength range, the latter is more compatible with the actual situation of track irregularity in China compared with the former. Thus, the Chinese high-speed railway ballastless track spectrum was adopted in this study. The track spectrum segmental fitting equation is as follows [28]:

$$S(f)=\frac{A}{f^n}, \tag{16}$$

where $S(f)$ denotes the spatial-frequency irregularity spectrum and f denotes the spatial frequency. A and n are the fitting coefficients, and their values have been given in literature [28].

When the speed of the HST is V, $F=Vf$ and $S(F)dF=S(f)df$. F is the time frequency, and $S(F)$ denotes the time-frequency irregularity spectrum.

$$S(F)=S(f)\cdot\frac{df}{F^n}=\frac{AV^{n-1}}{F^n}. \tag{17}$$

When V = 350 km/h, $L\in[L_{\min}, L_{\max}]$ = [2, 200] m, t = 100 s, the lateral alignment and cross level of track irregularity can be obtained by the frequency-domain method [2], as shown in Fig. 3.

Different track irregularities act on the four wheelsets at the same moment. Eq. (18) is derived based on the speed and structure parameters of the HST to improve the simulation accuracy.

$$\begin{cases} y_{ai}(t)=y_a(t-\tau_i) \\ \theta_{ci}(t)=\theta_c(t-\tau_i) \end{cases}, \tag{18}$$

where l_t denotes half of the wheelbase of the bogie, l_c denotes half of the fixed distance of the car body, y_a is the lateral alignment of track irregularity, and θ_c is the cross level of track irregularity. $\tau_1=0, \tau_2=2l_t/V, \tau_3=2l_c/V, \tau_4=2(l_t+l_c)/V$.

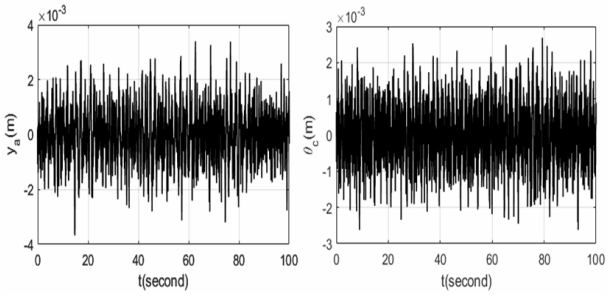

(a) Lateral alignment of track irregularity (b) Cross level of track irregularity

Fig. 3. Chinese high-speed railway ballastless track spectrum.

2.2 Problem formulation

Eqs. (8)-(15) can be used to present the state space model of HST as follows:

$$\begin{cases} \dot{\mathbf{x}}_0=\mathbf{A}_0\mathbf{x}_0+\mathbf{B}_0\mathbf{u} \\ \mathbf{y}_0=\mathbf{C}_0\mathbf{x}_0+\mathbf{D}_0\mathbf{u} \end{cases}, \tag{19}$$

where $\mathbf{x}_0=\begin{bmatrix} y_c,\phi_c,\psi_c,y_{t1},\phi_{t1},\psi_{t1},y_{t2},\phi_{t2},\psi_{t2},\dot{y}_c, \\ \dot{\phi}_c,\dot{\psi}_c,\dot{y}_{t1},\dot{\phi}_{t1},\dot{\psi}_{t1},\dot{y}_{t2},\dot{\phi}_{t2},\dot{\psi}_{t2},y_{w1}, \\ \psi_{w1},y_{w2},\psi_{w2},y_{w3},\psi_{w3},y_{w4},\psi_{w4}, \\ \dot{y}_{w1},\dot{\psi}_{w1},\dot{y}_{w2},\dot{\psi}_{w2},\dot{y}_{w3},\dot{\psi}_{w3},\dot{y}_{w4},\dot{\psi}_{w4} \end{bmatrix}^{\mathrm{T}}$, $\mathbf{u}=[F_{l1},F_{r1},F_{l2},F_{r2}]^{\mathrm{T}}$.

This problem can be described as a control strategy to dynamically adjust the actuator control force (***u***), which in turn reduces the lateral vibration of the HST car body and bogie. Then, the lateral running stability and safety of the HST are improved. Therefore, the design of a control strategy to decrease the HST car body's lateral vibration is the main objective of this study.

2.3 Model validation

HST line testing is expensive and requires permission from relevant authorities. Nowadays, the multibody dynamics software Simpack is mainly used to simulate HST motion, and Simpack simulation data are employed as validation data. The HST lateral vibration model in this study was established using Simpack and Simulink to verify the validity of the proposed model. The lateral displacement, roll angle, and yaw angle of the car body were obtained by simulation, as shown in Fig. 4.

In Fig. 4, the change rules of the lateral displacement, roll angle, and yaw angle of the car body obtained by Simpack and Simulink are nearly the same. The amplitude of the car body lateral displacement is slightly different due to the unavoidable difference in the wheel–rail forces in Simpack and Simulink. In this study, anti-yaw dampers were added to the classical model. The anti-yaw damper only affects the yaw motion of the car body. Fig. 4(c) shows that the change rule and amplitude of the car body yaw angle remain consistent, proving the validity of the proposed model.

3. MPC strategy design

Compared with PID and LQR, MPC adopts the rolling optimization strategy, which has strong robustness and antidisturbance ability. However, during the operation of the HST, wheel–rail contact exhibits strong nonlinearity, so establishing an accurate mathematical model of wheel–rail contact is diffi-

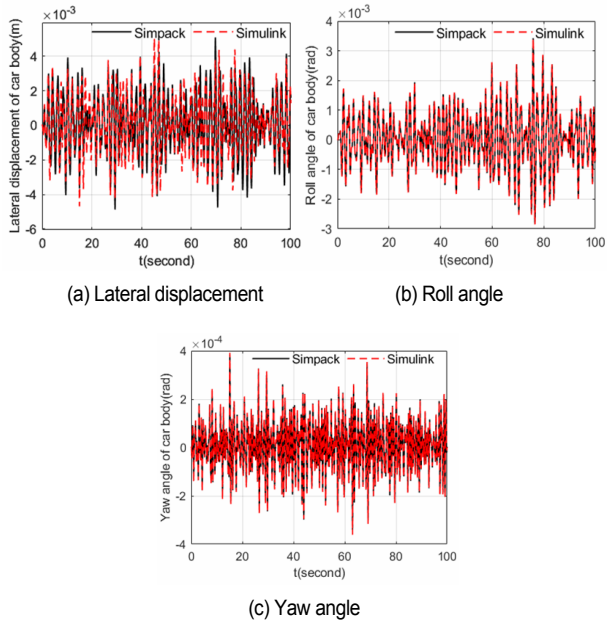

(a) Lateral displacement (b) Roll angle

(c) Yaw angle

Fig. 4. Lateral displacement, roll angle, and yaw angle of the car body.

cult. In this study, the lateral and yaw motions of HST wheelsets were adopted as disturbance inputs to solve this problem. Then, the 17-DOF lateral vibration model was simplified to a 9-DOF model with the following state space equation:

$$\begin{cases} \dot{\mathbf{x}} = \mathbf{A}_c\mathbf{x} + \mathbf{B}_c\mathbf{u} + \mathbf{G}_c\mathbf{d} \\ \mathbf{y} = \mathbf{C}_c\mathbf{x} \end{cases}, \tag{20}$$

where $\mathbf{A}_c \in R^{18\times18}$ denotes the state matrix, $\mathbf{B}_c \in R^{18\times4}$ is the control input matrix, $\mathbf{G}_c \in R^{18\times16}$ is the wheelset disturbance input matrix, and $\mathbf{C}_c \in I^{18\times18}$ denotes the output matrix.

$$\mathbf{x} = \begin{bmatrix} y_c, \phi_c, \psi_c, y_{t1}, \phi_{t1}, \psi_{t1}, y_{t2}, \phi_{t2}, \psi_{t2}, \\ \dot{y}_c, \dot{\phi}_c, \dot{\psi}_c, \dot{y}_{t1}, \dot{\phi}_{t1}, \dot{\psi}_{t1}, \dot{y}_{t2}, \dot{\phi}_{t2}, \dot{\psi}_{t2} \end{bmatrix}^{\mathrm{T}}$$

$$\mathbf{d} = \begin{bmatrix} y_{w1}, \psi_{w1}, y_{w2}, \psi_{w2}, y_{w3}, \psi_{w3}, y_{w4}, \psi_{w4}, \\ \dot{y}_{w1}, \dot{\psi}_{w1}, \dot{y}_{w2}, \dot{\psi}_{w2}, \dot{y}_{w3}, \dot{\psi}_{w3}, \dot{y}_{w4}, \dot{\psi}_{w4} \end{bmatrix}^{\mathrm{T}}$$

Then, the discrete state space model given in Eq. (21) was obtained by discretizing the equation with a zero-order holder [18].

$$\begin{cases} \mathbf{x}(k+1) = \mathbf{A}\mathbf{x}(k) + \mathbf{B}\mathbf{u}(k) + \mathbf{G}\mathbf{d}(k) \\ \mathbf{y}(k) = \mathbf{C}\mathbf{x}(k) \end{cases}, \tag{21}$$

where $\mathbf{A} = \exp^{\mathbf{A}_c T_s}$, $\mathbf{B} = \int_0^{T_s} \exp^{\mathbf{A}_c t}\mathbf{B}_c dt$, $\mathbf{G} = \int_0^{T_s} \exp^{\mathbf{A}_c t}\mathbf{G}_c dt$, $\mathbf{C} = \mathbf{C}_c$. T_s denotes the sampling period.

3.1 MPC design

3.1.1 Predictive model

The predicted state based on time *k* is shown in Eq. (21).

$$\begin{cases} \mathbf{x}(k+1|k) = \mathbf{A}\mathbf{x}(k) + \mathbf{B}\mathbf{u}(k) + \mathbf{G}\mathbf{d}(k) \\ \mathbf{x}(k+2|k) = \mathbf{A}\mathbf{x}(k) + \mathbf{A}\mathbf{B}\mathbf{u}(k) + \mathbf{B}\mathbf{u}(k+1) \\ \qquad + \mathbf{A}\mathbf{G}\mathbf{d}(k) + \mathbf{G}\mathbf{d}(k+1) \\ \vdots \\ \mathbf{x}(k+p|k) = \mathbf{A}^p\mathbf{x}(k) + \mathbf{A}^{p-1}\mathbf{B}\mathbf{u}(k) + \cdots \\ \qquad + \mathbf{A}^{p-m}\mathbf{B}\mathbf{u}(k+m-1) + \cdots + \mathbf{B}\mathbf{u}(k+p-1) \\ \qquad \cdots + \mathbf{A}^{p-1}\mathbf{G}\mathbf{d}(k) + \cdots + \mathbf{A}^{p-m}\mathbf{G}\mathbf{d}(k+m-1) \\ \qquad + \cdots + \mathbf{G}\mathbf{d}(k+p-1) \\ \mathbf{u}(k+j|k) = \mathbf{u}(k+m-1|k) \ (j = m, m+1, \ldots, p-1) \end{cases}, \tag{22}$$

where *p* denotes the prediction horizon, m denotes the control horizon, and *p* > *m*.

$$\begin{cases} \mathbf{Y} = \left[\mathbf{y}^{\mathrm{T}}(k+1|k) \quad \mathbf{y}^{\mathrm{T}}(k+2|k) \quad \cdots \quad \mathbf{y}^{\mathrm{T}}(k+p|k)\right]^{\mathrm{T}} \\ \mathbf{U} = \left[\mathbf{u}^{\mathrm{T}}(k|k) \quad \mathbf{u}^{\mathrm{T}}(k+1|k) \quad \cdots \quad \mathbf{u}^{\mathrm{T}}(k+p-1|k)\right]^{\mathrm{T}} \\ \mathbf{D} = \left[\mathbf{d}^{\mathrm{T}}(k) \quad \mathbf{d}^{\mathrm{T}}(k+1) \quad \cdots \quad \mathbf{d}^{\mathrm{T}}(k+p-1)\right]^{\mathrm{T}}. \end{cases} \tag{23}$$

In accordance with Eq. (23), the prediction model, Eq. (24), can be obtained.

$$\mathbf{Y} = \mathbf{S}_x\mathbf{x}(k) + \mathbf{S}_u\mathbf{U} + \mathbf{S}_d\mathbf{D}, \tag{24}$$

where $\mathbf{S}_x = \begin{bmatrix} \mathbf{CA} \\ \mathbf{CA}^2 \\ \vdots \\ \mathbf{CA}^p \end{bmatrix}$, $\mathbf{S}_u = \begin{bmatrix} \mathbf{CB} & 0 & \cdots & 0 \\ \mathbf{CAB} & \mathbf{CB} & \cdots & 0 \\ \vdots & \vdots & \ddots & \vdots \\ \mathbf{CA}^{p-1}\mathbf{B} & \mathbf{CA}^{p-2}\mathbf{B} & \cdots & \mathbf{CB} \end{bmatrix}$, $\mathbf{S}_d = \begin{bmatrix} \mathbf{CG} & 0 & \cdots & 0 \\ \mathbf{CAG} & \mathbf{CG} & \cdots & 0 \\ \vdots & \vdots & \ddots & \vdots \\ \mathbf{CA}^{p-1}\mathbf{G} & \mathbf{CA}^{p-2}\mathbf{G} & \cdots & \mathbf{CG} \end{bmatrix}$.

3.1.2 Objective function design

Eq. (20) shows that the system outputs are similar to the system state variables. The control goal is to make the system outputs approach zero at each moment under the minimum control force. Therefore, the following objective function was designed:

$$J(k) = \sum_{i=1}^{p}\left\|\mathbf{y}_d(k+i) - \mathbf{y}(k+i|k)\right\|_{\bar{\mathbf{Q}}}^2 + \sum_{i=1}^{p}\left\|\mathbf{u}(k+i-1|k)\right\|_{\bar{\mathbf{R}}}^2, \tag{25}$$

where $\mathbf{y}_d(k+i) = 0$ denotes the desired output at time *k+i*. $\bar{\mathbf{Q}} \geq 0$, $\bar{\mathbf{R}} > 0$ are positive definite symmetric weight matrices. For arbitrary variable ζ and nonnegative matrix $\bar{M}$, $\|\zeta\|_{\bar{M}}^2 \equiv \zeta^{\mathrm{T}}\bar{M}\zeta$. The weight matrices are set as $\bar{\mathbf{R}} = diag\{0.001,0.001,0.001,0.001,0.001\}$, $\bar{\mathbf{Q}} = diag\{100, 100, 1000, 1, 1, 1, 1, 1, 1, 100000, 100000, 1000000, 1, 1, 1, 1, 1, 1\}$.

However, the saturation and delay of the actuator are un-

avoidable. As a result, the actuator can only provide limited force to HST. The control input amplitude constraint is defined as follows to ensure that the control strategy can be used in engineering.

$$s.t. \quad \mathbf{U}_{\min} \le \mathbf{U} \le \mathbf{U}_{\max}, \tag{26}$$

where $\boldsymbol{U}_{\min} = \left[u_{0,\min}^{\mathrm{T}} \quad u_{1,\min}^{\mathrm{T}} \quad \cdots \quad u_{m-1,\min}^{\mathrm{T}}\right]^{\mathrm{T}}$, $\boldsymbol{U}_{\max} = \left[u_{0,\max}^{\mathrm{T}} \quad u_{1,\max}^{\mathrm{T}} \quad \cdots \quad u_{m-1,\max}^{\mathrm{T}}\right]^{\mathrm{T}}$.

Then, the control goal can be expressed as

$$\min\{J(k)\} = \min\left\{\sum_{i=1}^{p}\left\|\mathbf{y}_d(k+i) - \mathbf{y}(k+i|k)\right\|_{\bar{\mathbf{Q}}}^2 + \sum_{i=1}^{p}\left\|\mathbf{u}(k+i-1|k)\right\|_{\bar{\mathbf{R}}}^2\right\}. \tag{27}$$
$$s.t. \quad \mathbf{U}_{\min} \le \mathbf{U} \le \mathbf{U}_{\max}$$

3.2 DOB design

3.2.1 DOB model

DOBs, which are widely used, provide a good way to observe uncertain disturbances. In previous research, DOBs were used for robot trajectory tracking [29, 30] and power system current tracking [31, 32]. The results indicated that DOBs can accurately track the reference signal. Inspired by these results, we designed a DOB to estimate the lateral motions of the HST wheelsets.

With Eq. (20), we obtain

$$\mathbf{G}_c\mathbf{d} = \dot{\mathbf{x}} - \mathbf{A}_c\mathbf{x} - \mathbf{B}_c\mathbf{u}. \tag{28}$$

Then, we introduce the system auxiliary variable (z) and design the following DOB.

$$\begin{cases}\hat{\mathbf{d}} = \mathbf{z} + \mathbf{L}(\mathbf{x})\mathbf{x} \\ \dot{\mathbf{z}} = -\mathbf{L}(\mathbf{x})\left[\mathbf{G}(\mathbf{L}(\mathbf{x})\mathbf{x} + \mathbf{z}) + \mathbf{A}\mathbf{x} + \mathbf{B}\mathbf{u}\right]\end{cases}, \tag{29}$$

where $\mathbf{z}$ denotes the system auxiliary variable, $\hat{\mathbf{d}} = \left[\hat{d}_1, \cdots, \hat{d}_{18}\right]^{\mathrm{T}}$ is the observed value of HST wheelset disturbance ($\mathbf{d}$), and $\mathbf{L}(\mathbf{x})$ denotes the DOB gain matrix.

3.2.2 DOB stability analysis

The DOB estimation error is defined as $\tilde{\mathbf{d}} = \mathbf{d} - \hat{\mathbf{d}}$. The estimation error derivative is obtained as follows:

$$\begin{aligned}\dot{\tilde{\mathbf{d}}} &= \dot{\mathbf{d}} - \dot{\hat{\mathbf{d}}} = \dot{\mathbf{d}} - (\dot{\mathbf{z}} + \mathbf{L}(\mathbf{x})\dot{\mathbf{x}}) \\ &= \dot{\mathbf{d}} - \mathbf{L}\left[\mathbf{G}(\mathbf{L}(\mathbf{x})\mathbf{x} + \mathbf{z}) + \mathbf{A}\mathbf{x} + \mathbf{B}\mathbf{u}\right]. \\ &= \dot{\mathbf{d}} - \mathbf{L}(\mathbf{x})\mathbf{G}(\mathbf{d} - \hat{\mathbf{d}}) = \dot{\mathbf{d}} - \mathbf{L}(\mathbf{x})\mathbf{G}\tilde{\mathbf{d}}\end{aligned} \tag{30}$$

When HST is running, the wheelset disturbance ($\mathbf{d}$) is bounded, and its variation is slow relative to HST speed, that is, $\|\mathbf{d}\| \le \mathbf{d}_M$, $\dot{\mathbf{d}} \approx 0$. Then, Eq. (30) can be rewritten as

$$\dot{\tilde{\mathbf{d}}} + \mathbf{L}\mathbf{G}\tilde{\mathbf{d}} = 0. \tag{31}$$

The Lyapunov function is defined as $V(\tilde{\mathbf{d}}) = \frac{1}{2}\tilde{\mathbf{d}}^{\mathrm{T}}\tilde{\mathbf{d}} \ge 0$ and V (0) = 0.

$$\dot{V}(\tilde{\mathbf{d}}) = \tilde{\mathbf{d}}^{\mathrm{T}}\dot{\tilde{\mathbf{d}}} = -\tilde{\mathbf{d}}^{\mathrm{T}}\mathbf{L}\mathbf{G}\tilde{\mathbf{d}}. \tag{32}$$

A reasonable $\mathbf{L}(\mathbf{x})$ [33] ensures that $\dot{V}(\tilde{\mathbf{d}}) \le 0$ and $\dot{V}$ (0) = 0, which can guarantee the stability of DOB.

3.3 MPC with DOB

By replacing $\mathbf{D}$ in Eq. (24) with $\hat{\mathbf{D}}$, we obtained the prediction model with DOB as follows:

$$\hat{\mathbf{Y}} = \mathbf{S}_x\mathbf{x}(k) + \mathbf{S}_u\mathbf{U} + \mathbf{S}_d\hat{\mathbf{D}}, \tag{33}$$

where $\hat{\mathbf{D}} = \left[\hat{\mathbf{d}}^{\mathrm{T}}(k) \quad \hat{\mathbf{d}}^{\mathrm{T}}(k+1) \quad \cdots \quad \hat{\mathbf{d}}^{\mathrm{T}}(k+p-1)\right]^{\mathrm{T}}$.

As shown in Fig. 5, the track irregularities (lateral alignment and cross level), uncertainty disturbances (turnout irregularity and aerodynamic load), and MPC control forces were simultaneously applied to HST. Acceleration sensors were used to measure the lateral acceleration of the HST car body and bogie. The lateral displacement speed, roll angular speed, yaw angular speed, lateral displacement, roll angle, and yaw angle of the HST car body and bogie center were obtained by first and second integration. Then, the system output (***y***) was obtained and is shown in Fig. 5. The DOB estimates $\hat{\mathbf{d}}$ were based on ***y*** and ***u***. In addition, MPC was utilized to provide an optimal ***u*** to reduce the lateral vibration of the HST car body on the basis of ***y***, $\hat{\mathbf{d}}$ and *Ref*.

In accordance with the requirements of GB/T 5599-2019 (Specification for Dynamic Performance Assessment and Testing Verification of Rolling Stock) [34], the acceleration sensor measurement points were arranged in the position shown in

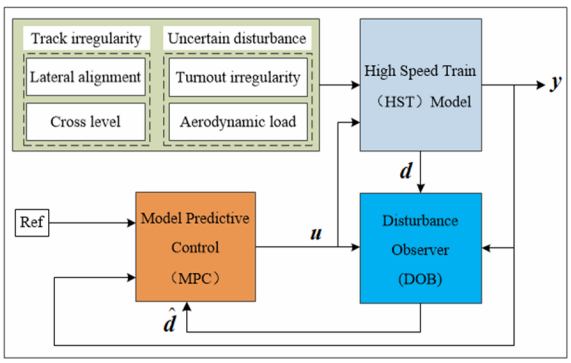

Fig. 5. Structure diagram of MPC for HST lateral vibration with DOB.

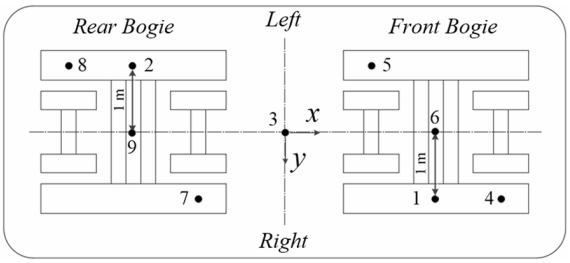

Fig. 6. Acceleration sensor measurement point layout.

Fig. 6. Measurement points 1, 2, and 3 measured the lateral acceleration at the front, rear, and center of the HST car body, respectively. Measurement points 4, 5, and 6 measured the lateral acceleration at the front, rear, and center of the HST front bogie, respectively. Measurement points 7, 8, and 9 measured the lateral acceleration at the front, rear, and center of the HST rear bogie, respectively.

3.4 Control effect analysis

In consideration of the difficulty and high cost of HST experiments, the numerical simulation method was adopted, and the simulation model was established by Simulink. With the track irregularities in Sec. 2.1.3 as the input of the simulation model, the motion data of the HST car body, bogie, and wheelset were obtained by simulation.

3.4.1 DOB observation effect

DOB was used to estimate the lateral displacement and speed, yaw angle, and angular speed of the four wheelsets, and the observation effect was judged by the estimation error. The lateral displacement and speed, yaw angle, angular speed, and estimation errors of the four wheelsets at 350 km/h are shown in Figs. 7 and 8.

As indicated in Figs. 7 and 8, the maximum lateral displacement estimation errors of the four wheelsets were 1.297×10^{-4}, 7.671×10^{-5}, 1.305×10^{-4}, and 7.757×10^{-5} m. The maximum yaw angle estimation errors of the four wheelsets were 1.141×10^{-4}, 1.030×10^{-4}, 1.105×10^{-4}, and 1.007×10^{-4} rad. However, the maximum lateral speed estimation errors of the four wheelsets were 4.435×10^{-3}, 4.717×10^{-3}, 4.453×10^{-3}, and 4.223×10^{-3} m/s. The maximum yaw angular speed estimation errors of the four wheelsets were 6.886×10^{-3}, 7.436×10^{-3}, 6.885×10^{-3}, and 7.052×10^{-3} rad/s.

The results showed that the estimation errors of the four wheelsets were small, indicating that DOB had a good observation effect.

3.4.2 MPC control effect

In Figs. 9 and 10, PC denotes passive control, and MPC denotes model predictive control. As indicated in Fig. 9, the peak value and root mean square (RMS) value of lateral acceleration at the rear end of the HST car body were greater than those at the front end of the HST car body under PC. However,

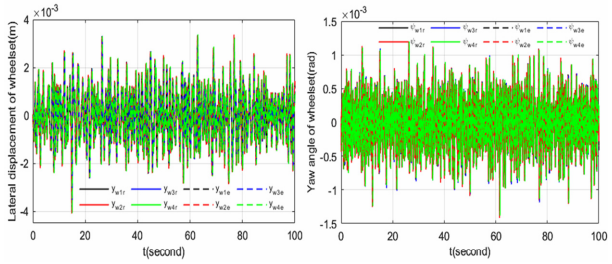

(a) Lateral displacement (b) Yaw angle

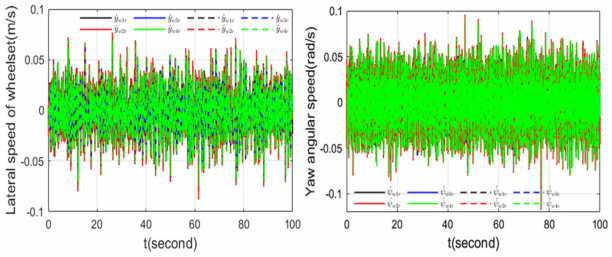

(c) Lateral speed (d) Yaw angular speed

Fig. 7. Lateral displacement and speed, yaw angle, and angular speed of the four wheelsets.

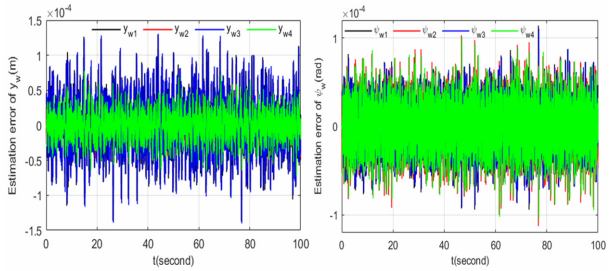

(a) Lateral displacement error (b) Yaw angle error

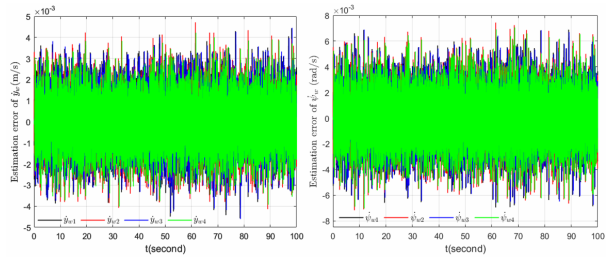

(c) Lateral speed error (d) Yaw angular speed error

Fig. 8. Estimation errors of the four wheelsets.

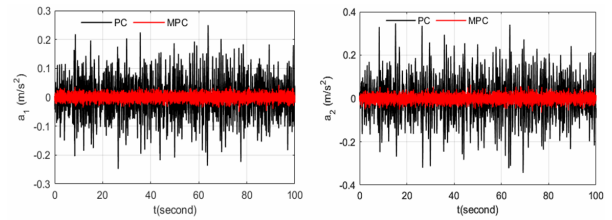

(a) Front end of the car body (b) Rear end of the car body

Fig. 9. Time-domain diagram of the lateral acceleration of the HST car body.

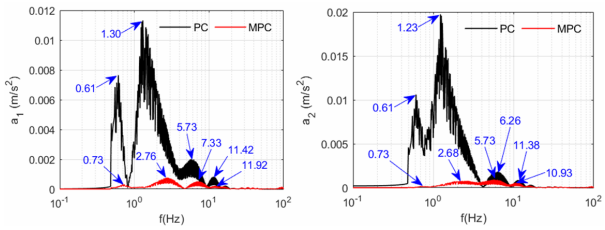

(a) Front end of the car body (b) Rear end of the car body

Fig. 10. Spectrum diagram of the lateral acceleration of the HST car body.

the peak and RMS values of lateral acceleration at the front and rear ends of the car body were similar under MPC. Compared with the peak and RMS values of PC, the peak and RMS values of MPC were considerably reduced. As shown in Fig. 10, the lateral vibration frequencies at the front end of the HST car body were 0.61, 1.30, 5.73 and 11.42 Hz under PC, and the main vibration frequency was 1.30 Hz, which shows the low-frequency yaw vibration of the HST car body. In addition, the lateral vibration frequencies at the rear end of the HST car body were 0.61, 1.23, 6.26 and 11.38 Hz, and the main vibration frequency was 1.23 Hz, which also shows the low-frequency yaw vibration of the HST car body. The vibration peaks appeared at 5.73 and 6.26 Hz at the front and rear ends of the HST car body, respectively, which reveals the serpentine vibration of the HST bogie [35].

However, the lateral vibration frequencies at the front end of the HST car body were 0.73, 2.76, 7.33 and 11.92 Hz under MPC, and the main vibration frequency was 2.76 Hz. The lateral vibration frequencies at the rear end of the HST car body were 0.73, 2.68, 5.73 and 10.93 Hz under MPC, and the main vibration frequency was 2.68 Hz. Compared with PC, MPC could considerably reduce the lateral vibration of the HST car body over a wide frequency range. The lateral vibration accelerations of the HST car body and bogie under PC and MPC are shown in Table 2.

As shown in Table 2, compared with PC, MPC reduced the peak and RMS values of lateral acceleration at the front end of the HST car body by 79.70 % and 87.59 %, respectively, and the peak and RMS values of lateral acceleration at the rear end of the HST car body decreased by 81.10 % and 87.04 %, respectively. On the contrary, MPC increased the peak and RMS values of lateral acceleration at the front end of the front bogie by 23.98 % and 14.99 %, respectively, and the peak and RMS values of the rear end of the front bogie increased by 19.56 % and 13.56 %, respectively. In addition, MPC reduced the peak and RMS values of lateral acceleration at the front end of the rear bogie by 8.27 % and 3.93 %, respectively, and the peak and RMS values of lateral acceleration at the rear end of the rear bogie changed only slightly. These results verify that MPC could considerably reduce the lateral vibration of the HST car body without remarkably increasing the peak and RMS values of bogie lateral acceleration. Therefore, MPC with DOB can be used to improve the lateral stability of HST car body.

Table 2. Lateral vibration accelerations of the HST car body and bogie.

	PC		MPC		Rate of change	
	Peak	RMS	Peak	RMS	Peak	RMS
Front end of the car body	0.2497	0.0677	0.0507	0.0084	-79.70 %	-87.59 %
Rear end of the car body	0.3471	0.0988	0.0656	0.0128	-81.10 %	-87.04 %
Front end of the front bogie	1.1220	0.2335	1.3910	0.2685	23.98 %	14.99 %
Rear end of the front bogie	1.1860	0.2411	1.4180	0.2738	19.56 %	13.56 %
Front end of the rear bogie	1.2460	0.2573	1.1430	0.2472	-8.27 %	-3.93 %
Rear end of the rear bogie	1.3120	0.2633	1.3080	0.2683	-0.30 %	1.90 %

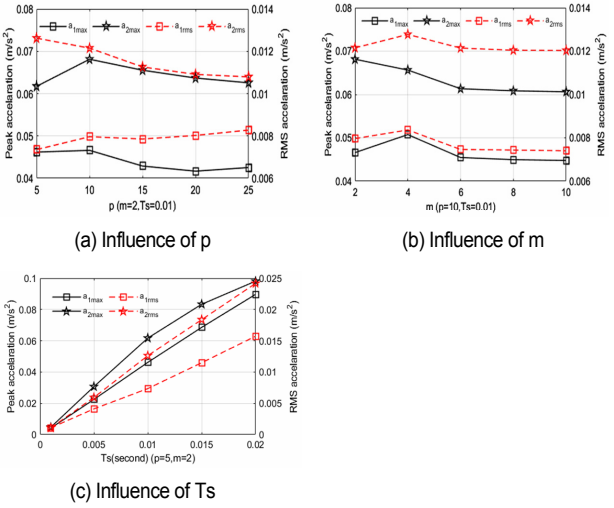

(a) Influence of p (b) Influence of m

(c) Influence of Ts

Fig. 11. Influence of MPC parameters on the lateral vibration acceleration of the HST car body.

4. CMPC strategy design

Calculation effort and iterative calculation time are the key factors that affect the application of MPC. High computation effort requires high-performance data processing equipment, and long iteration calculation time causes a serious delay in actuator actions, which may diminish or even worsen the actual control effect. We studied the effects of MPC parameters, including prediction horizon (p), control horizon (m), and sampling period (Ts), on the lateral vibration acceleration of the HST car body and the iterative calculation time of MPC. Then, we designed the CMPC controller.

4.1 Influence of MPC parameters

In Fig. 11, a_{1max}, a_{2max}, a_{1rms}, and a_{2rms} denote the peak and RMS values of lateral acceleration at the front and rear ends of the HST car body, respectively. When m = 2, Ts = 0.01 s, and

p increased from 5 to 25, the peak value of lateral acceleration at the front and rear ends of the car body increased first and then decreased. The RMS value of lateral acceleration at the front end of the HST car body increased slowly, and the RMS value of lateral acceleration at the rear end of the HST car body decreased gradually. Therefore, increasing p appropriately can reduce the lateral vibration acceleration of the HST car body. When p = 10, Ts = 0.01 s, and m increased from 2 to 10, the peak and RMS values of lateral acceleration at the front end of the HST car body increased then decreased, and the RMS value of lateral acceleration at the rear end of the HST car body increased then decreased. However, the peak value of lateral acceleration at the rear end of the HST car body decreased gradually. When p = 5 and m = 2, the peak and RMS values of lateral vibration acceleration at the front and rear ends of the HST car body increased with the increase in Ts. Therefore, decreasing Ts can reduce the lateral vibration acceleration of the HST car body.

As shown in Fig. 12, the iteration calculation time increased with the increase in p and m and decreased with the increase in Ts. The results in Figs. 11 and 12 indicate that the effects of p, m and Ts on the lateral vibration acceleration of the HST car body and iteration calculation time were contradictory. In practical engineering application, p, m and Ts must be matched to ensure that MPC can effectively reduce the lateral vibration of the HST car body.

4.2 CMPC with DOB

In consideration of the contradictory effects of p, m and Ts on the lateral vibration acceleration of the HST car body and iterative calculation time and the difficulty of engineering implementation, a novel CMPC strategy with DOB for lateral vibration of HST was proposed, and its structure is shown in Fig. 13.

CMPC consists of MPC1 and MPC2. MPC1 and MPC2 have the same prediction models but different parameters. MPC1 adopts $p_1 = 10$, $m_1 = 6$, and $Ts_1 = 0.005$, and MPC2 uses $p_2 = 5$, $m_2 = 2$, and $Ts_2 = 0.02$. The control idea of CMPC is to use large p and m values and a small Ts when the lateral vibration acceleration of the HST car body is large to quickly reduce the lateral vibration acceleration of the HST car body. In addition, small p and m and large Ts are used when the lateral vibration acceleration of the car body is small to shorten the iterative calculation time. In other words, the purpose of CMPC is to achieve a reasonable match between the lateral vibration acceleration of the HST car body and the iterative calculation time of MPC. The control force (**u**) of CMPC was designed as follows.

$$\mathbf{u} = \begin{cases} \mathbf{u}_1 & \max\{\,|a_1|,\ |a_2|\,\} \geq a_{c0} \\ \mathbf{u}_2 & \max\{\,|a_1|,\ |a_2|\,\} < a_{c0} \end{cases}, \tag{34}$$

where a_1 and a_2 are the lateral vibration accelerations at the front and rear ends of the HST car body, respectively, and a_{c0} is the threshold value for the lateral vibration acceleration of the HST car body. Through extensive numerical simulation, we set $a_{c0} = 0.01$.

4.3 CMPC control effect

In accordance with the lateral stability index calculation formula in a relevant specification [34], the lateral stability index was calculated every five seconds on the basis of the lateral vibration acceleration of the HST car body. The calculation results are shown in Fig. 15.

In Table 3, T denotes the iteration calculation time, a_1 is the lateral acceleration at the front end of the car body, a_2 is the lateral acceleration at the rear end of the car body, L_1 refers to the lateral stability index at the front end of the car body, and L_2 denotes the lateral stability index at the rear end of the car body.

Figs. 14, 15, and Table 3 show that under CMPC, the peak and RMS values of lateral vibration acceleration at the front and rear ends of the HST car body were between the values for MPC1 and MPC2 but close to the value for MPC1. In addition, the iterative calculation time of CMPC was 23.75 s, which

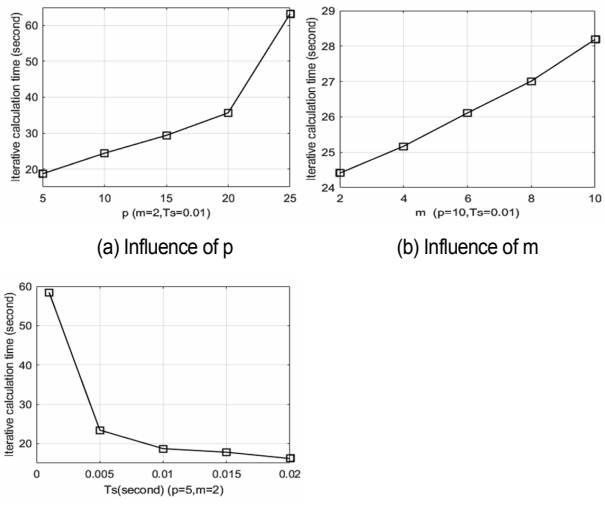

(a) Influence of p (b) Influence of m

(c) Influence of Ts

Fig. 12. Influence of MPC parameters on iterative calculation time.

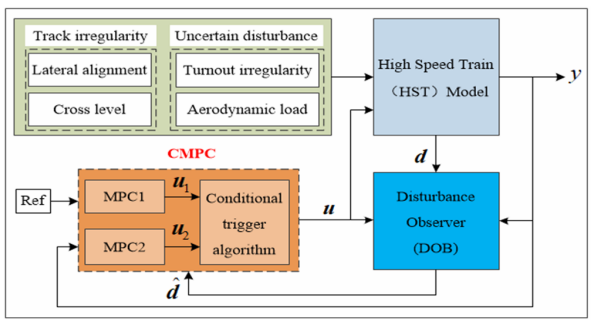

Fig. 13. Structure diagram of CMPC for HST lateral vibration with DOB.

Table 3. Control effects under different controllers.

	T (s)	a_1 (m/s^2)		L_1	a_2 (m/s^2)		L_2
		Peak	RMS	Peak	Peak	RMS	Peak
MPC1	42.50	0.0160	0.0032	0.6066	0.0271	0.0049	0.7436
CMPC	23.75	0.0315	0.0070	0.8024	0.0385	0.0099	0.9257
MPC2	16.18	0.0897	0.0157	1.0539	0.0982	0.0242	1.2317

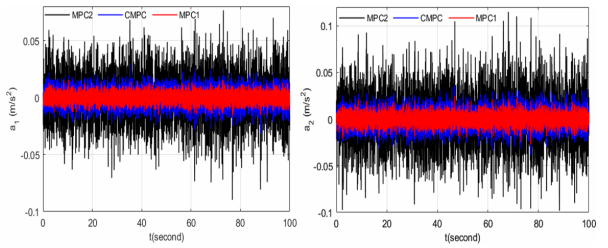

(a) Front end of the car body (b) Rear end of the car body

Fig. 14. Lateral vibration acceleration of the HST car body under different controllers.

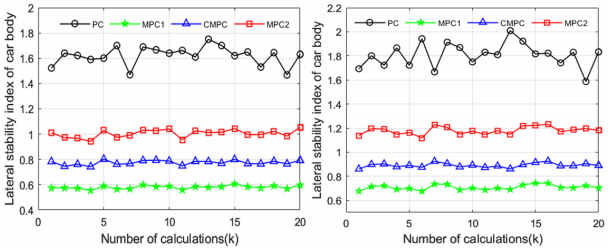

(a) Front end of the car body (b) Rear end of the car body

Fig. 15. Lateral stability index of the HST car body under different controllers.

was about half of the time for MPC1. These results verify the rationality and effectiveness of CMPC.

5. Verification of CMPC robustness

The simulation results show that CMPC can considerably reduce the peak and RMS values of lateral acceleration at the front and rear ends of the HST car body when HST is only excited by track irregularities. However, complex working conditions, such as changing speed, passing through turnouts, and meeting inside and outside of tunnels, arise during HST operation. Therefore, studying the control effect of CMPC under complex working conditions is meaningful.

5.1 Influence of speed

As shown in Fig. 16, when the speed increased from 250 km/h to 450 km/h, the lateral stability indexes at the front and rear ends of the HST car body gradually increased. The lateral stability index of the front end of the HST car body increased at a higher rate compared with the lateral stability index of the rear end of the HST car body, and the increase was

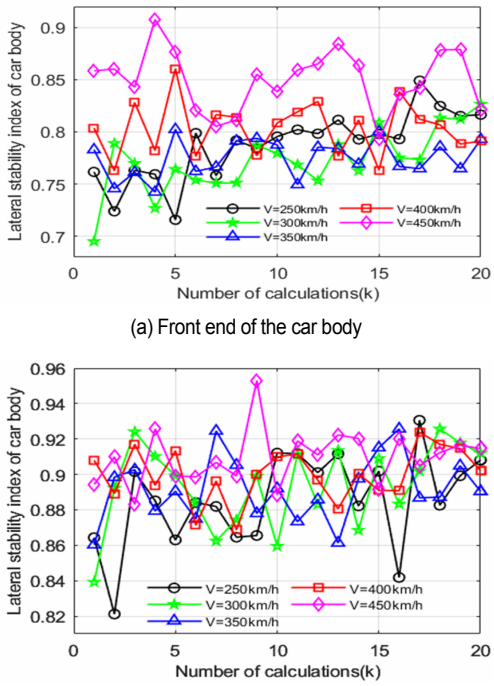

(a) Front end of the car body

(b) Rear end of the car body

Fig. 16. Lateral stability index of the car body under different speeds.

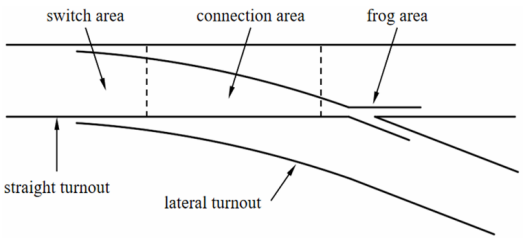

Fig. 17. Schematic of the railway turnout.

highly obvious when the speed was 450 km/h. Nevertheless, the lateral stability indexes at the front and rear ends of the HST car body did not exceed 1.0, which verifies that CMPC can maintain a good control effect when the HST speed changes.

5.2 Influence of turnout

5.2.1 Railway turnout irregularity simulation

A railway turnout is composed of switch, connection, and frog areas [36] and includes straight and lateral turnouts. In this study, a 60 kg/m steel rail and a No. 18 movable center track turnout were used. The total length of the turnout was 69 m, and the lengths of the switch, connection, and frog areas were 23, 27 and 19 m, respectively. In addition, the radius of the guide curve was 1100 m, the allowable passing speed in the straight turnout was 350 km/h, and that in the lateral turnout was 80 km/h. A schematic of the turnout is shown in Fig. 17. This study focused on CMPC's control effect when HST passes through the straight turnout. The control effect when

Table 4. Parameters of railway turnout irregularity.

Parameter	Switch area (i = 1)	Connection area (i = 2)	Frog area (i = 3)
L_i(m)	10	15	10
A_{ai}(m)	0.004	0.001	0.002
A_{ci}(m)	0.003	0.001	0.001

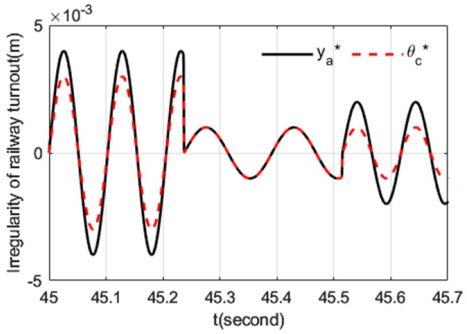

Fig. 18. Lateral alignment and cross level of railway turnout irregularity.

HST passes through the lateral turnout will be investigated in future research. Turnout irregularity can be equated to a periodic signal [37].

The lateral alignment and cross level of turnout irregularity are defined as sinusoidal signals and expressed as follows:

$$\begin{cases} y_{ai}^{*}(t) = A_{ai}\sin\dfrac{2\pi Vt}{L_i} \\ \theta_{ci}^{*}(t) = A_{ci}\sin\dfrac{2\pi Vt}{L_i} \end{cases}, \tag{35}$$

where y_{ai}^{*}, θ_{ci}^{*} denotes the lateral alignment and cross level of turnout irregularities in the switch, connection, and frog areas. A_{ai} and A_{ci} denote the amplitude coefficients, L_i is the wavelength, and V denotes HST speed.

The lateral alignment and cross level of railway turnout irregularity are shown in Fig. 18. The detailed parameters are given in Table 4.

5.2.2 Influence of turnout on the CMPC control effect

The track and turnout irregularities shown in Figs. 3 and 18 were applied to HST, and the speed was set to V = 350 km/h. Then, the lateral stability index curve of the HST car body was obtained by simulation, as shown in Fig. 19. When HST passed through the straight turnout, because of the short action time, the lateral stability indexes at the front and rear ends of the HST car body increased, but the increase was small. However, the lateral acceleration of the HST car body increased obviously, which in turn increased the operational safety risk of HST. Compared with PC, CMPC maintained the lateral stability index of the HST car body at a small value, which verifies that CMPC exerted a good control effect when HST passed through the straight railway turnout.

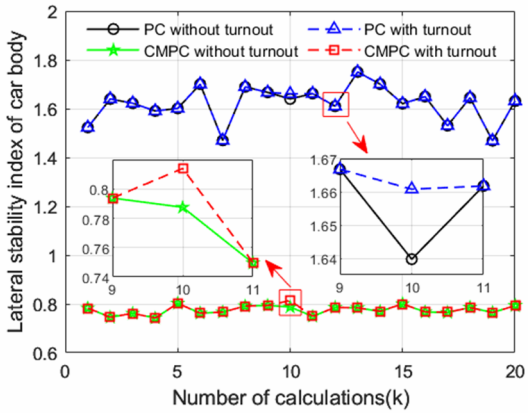

(a) Front end of the car body

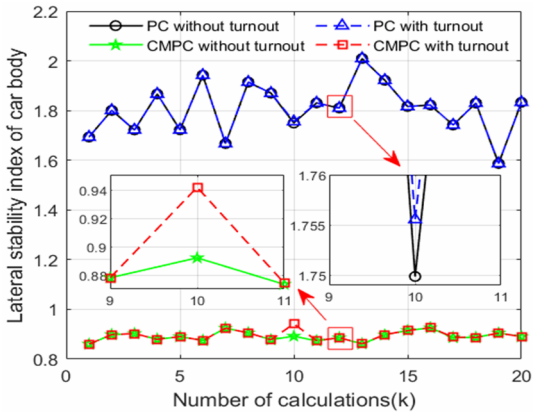

(b) Rear end of the car body

Fig. 19. Lateral stability index of the car body under turnout.

5.3 Influence of aerodynamic load

5.3.1 Aerodynamic load simulation

When two HSTs meet inside and outside a tunnel, a large aerodynamic load is generated. At the same speed, the aerodynamic load generated by the inside of the tunnel is greater than that generated by the outside of the tunnel. This study focused on the influence of the aerodynamic load inside the tunnel on the CMPC control effect. The dynamic offline simulation calculation method [38] was used to obtain the aerodynamic force and aerodynamic moment of two HSTs with a running speed of 350 km/h when they meet inside a tunnel with a length of 800 m. In Fig. 20, Fx, Fy and Fz refer to the longitudinal, lateral and vertical aerodynamic forces, respectively, and Mx, My and Mz are the roll, nod and yaw moments, respectively.

5.3.2 Influence of aerodynamic load on the CMPC control effect

The aerodynamic load shown in Fig. 20 and the track irregularity shown in Fig. 3 were applied to HST, and the lateral stability index curve of the HST car body shown in Fig.

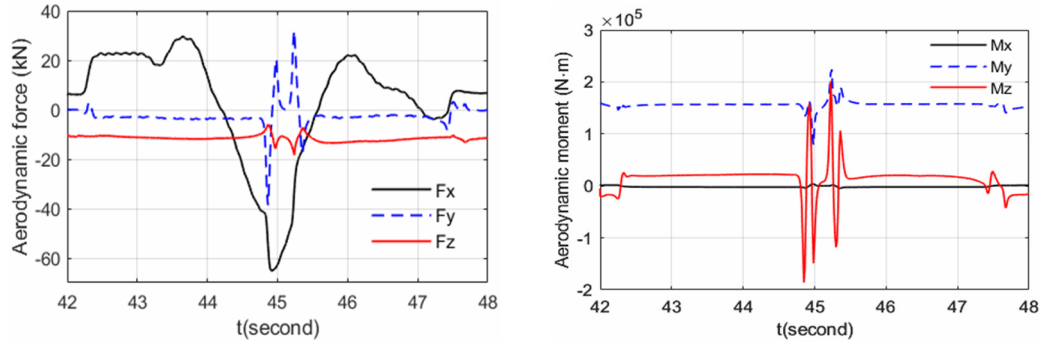

(a) Aerodynamic force (b) Aerodynamic moment

Fig. 20. Aerodynamic load inside the tunnel at 350 km/h.

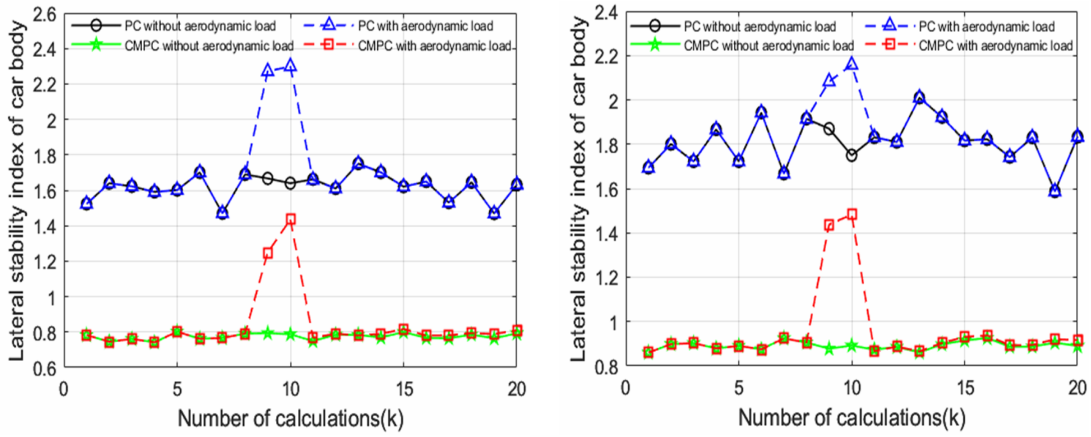

(a) Front end of the car body (b) Rear end of the car body

Fig. 21. Lateral stability index of the HST car body under aerodynamic load.

21 was obtained by simulation. As indicated in Fig. 20, when the two HSTs met inside the tunnel at a speed of 350 km/h, large aerodynamic forces and moments were generated. The peak values of Fx, Fy and Fz were 65, 38 and 18 kN, respectively, and the peak values of Mx, My and Mz were 3.7×10^3, 2.2×10^5 and 1.8×10^5 N•m, respectively. As shown in Fig. 21, the lateral stability index of the HST car body increased when the aerodynamic load was applied to HST, but the lateral stability index of the HST car body under CMPC was still smaller than that under PC, a result that verifies the advantages of CMPC.

6. Conclusions

An increase in speed decreases the lateral running stability of passive-controlled HSTs, and an accurate lateral vibration model and effective control strategy can improve HST lateral running stability. However, the more complex the model is, the more difficult the control strategy design is. In this study, an improved 17-DOF HST lateral vibration model that includes the anti-yaw damper was established. The Maxwell model of the anti-yaw damper was transformed into the Voigt model by using the equivalence method to ensure the accuracy of the model and reduce modeling difficulty.

The DOB adopted in this study could accurately estimate the lateral and yaw motions of the wheelsets. The maximum estimation errors for wheelset lateral displacement, lateral speed, yaw angle and yaw angular speed were 1.305×10^{-4} m, 4.717×10^{-3} m/s, 1.141×10^{-4} rad and 7.436×10^{-3} rad/s, respectively. In addition, DOB could transform the 17-DOF model into a 9-DOF model, thus making the design of the control strategy easy.

MPC with DOB could reduce the peak and RMS values of car body lateral vibration acceleration in a large frequency range, thus effectively improving the car body's lateral running stability. Although this strategy increased the peak and RMS values of bogie lateral vibration acceleration, which were much smaller than the bogie serpentine threshold, the results prove that the strategy can still be used.

CMPC with DOB reduced the peak and RMS values of car body lateral vibration acceleration and the iterative computation time, thus ensuring that the actuator could act effectively. When HSTs operate under complex working conditions, this strategy can still effectively improve the car body's lateral running stability, which verifies that the proposed strategy has a good control effect and potential for engineering application.

Acknowledgments

This work was supported by the National Natural Science Foundation of China (Nos. U2034210, 51975487, and 52372402).

References

[1] T. Jin et al., Theoretical and experimental investigation of a stiffness-controllable suspension for railway vehicles to avoid resonance, *International Journal of Mechanical Sciences*, 187 (2020) 105901.

[2] Q. Zhu, L. Li, C. Chen, C. Liu and G. Hu, A low-cost lateral active suspension system of the high-speed train for ride quality based on the resonant control method, *IEEE Transactions on Industrial Electronics*, 65 (5) (2018) 4187-4196.

[3] L. Zong, X. Gong, S. Xuan and C. Guo, Semi-active H∞control of high-speed railway vehicle suspension with magnetorheological dampers, *Vehicle System Dynamics*, 51 (5) (2013) 600-626.

[4] X. Wang, D. Huang, N. Qin, C. Chen and K. Zhang, Modeling and second-order sliding mode control for lateral vibration of high-speed train with MR dampers, *IEEE Transactions on Intelligent Transportation Systems*, 23 (8) (2022) 10299-10308.

[5] D. Huang, C. Chen, T. Huang, D. Zhao and Q. Tang, An active repetitive learning control method for lateral suspension systems of high-speed trains, *IEEE Transactions on Neural Networks and Learning Systems*, 31 (10) (2020) 4094-4103.

[6] Y. Yan, J. Zeng, C. Huang and T. Zhang, Bifurcation analysis of railway bogie with yaw damper, *Archive of Applied Mechanics*, 89 (7) (2019) 1185-1199.

[7] Z. Xia, J. Zhou, D. Gong, W. Sun and Y. Sun, Research on low-frequency lateral sway of railway vehicle body based on modal continuous tracking, *Journal of the China Railway Society*, 40 (12) (2018) 46-54.

[8] X. Zheng, A. Zolotas and R. Goodall, Combined active suspension and structural damping control for suppression of flexible bodied railway vehicle vibration, *Vehicle System Dynamics*, 58 (2) (2020) 198-228.

[9] Z. Gao, B. Tian, D. Wu and Y. Chang, Study on semi-active control of running stability in the high-speed train under unsteady aerodynamic loads and track excitation, *Vehicle System Dynamics*, 59 (1) (2021) 101-114.

[10] Y. Liao, Z. Chen, Y. Liu and Y. Zhao, Design and simulation analysis of a continuous mixed control for high-speed train suspension systems, *Journal of Vibration and Shock*, 40 (6) (2021) 235-242.

[11] B. A. Negash, W. You, J. Lee, C. Lee and K. Lee, Semi-active control of a nonlinear quarter-car model of hyperloop capsule vehicle with skyhook and mixed skyhook-acceleration driven damper controller, *Advances in Mechanical Engineering*, 13 (2) (2021) 1-14.

[12] S. Yang, Y. Zhao, Y. Liu, Y. Liao and P. Wang, A new semi-active control strategy on lateral suspension systems of high-speed trains and its application in HIL test rig, *Vehicle System Dynamics*, 61 (5) (2023) 1317-1344.

[13] Y. Wu, J. Zeng, H. Shi, B. Zhu and Q. Wang, A hybrid damping control strategy for high-speed trains running on existing tracks, *Journal of Low Frequency Noise Vibration and Active Control*, 41 (3) (2022) 1258-1271.

[14] S. Bhardawaj, R. C. Sharma and S. K. Sharma, Development of multibody dynamical using MR damper based semi-active bio-inspired chaotic fruit fly and fuzzy logic hybrid suspension control for rail vehicle system, *Proceedings of the Institution of Mechanical Engineers Part K-Journal of Multi-Body Dynamics*, 234 (4) (2020) 723-744.

[15] Q. Zhu, J. Ding and M. Yang, LQG control based lateral active secondary and primary suspensions of high-speed train for ride quality and hunting stability, *IET Control Theory and Applications*, 12 (10) (2018) 1497-1504.

[16] Y. Zeng, W. Zhang and D. Song, Lateral-vertical coupled active suspension on railway vehicle and optimal control methods, *Vehicle System Dynamics*, 60 (1) (2020) 258-280.

[17] E. D. Gialleonardo, A. Facchinetti and S. Bruni, Control of an integrated lateral and roll suspension for a high-speed railway vehicle, *Vehicle System Dynamics*, 61 (2) (2023) 472-498.

[18] Z. Li, Y. Ding, H. Yang and J. Liu, Generalized predictive control tuning for high-speed train based on controller matching method, *Ournal of the China Railway Society*, 40 (9) (2018) 82-89.

[19] Z. Li, L. Zhou, H. Yang and M. Ye, Iterative learning control method for EMUs based on predictive control, *Journal of Traffic and Transportation Engineering,* 23 (1) (2023) 280-290.

[20] Y. Wang, S. Zhu, S. Li, L. Yang and B. D. Schutter, Hierarchical model predictive control for on-line high-speed railway delay management and train control in a dynamic operations environment, *IEEE Transactions on Control Systems Technology*, 30 (6) (2022) 2344-2359.

[21] H. Zhang, S. Li, Y. Wang, Y. Wang and L. Yang, Real-time optimization strategy for single-track high-speed train rescheduling with disturbance uncertainties: A scenario-based chance-constrained model predictive control approach, *Computers & Operations Research*, 127 (2021) 105135.

[22] X. Xu, J. Peng, R. Zhang, B. Chen, F. Zhou, Y. Yang, K. Gao and Z. Huang, Adaptive model predictive control for cruise control of high-speed trains with time-varying parameters, *Journal of Advanced Transportation*, 2019 (2019) 1-11.

[23] Z. Sun, L. Dai, K. Liu, D. V. Dimarogonas and Y. Xia, Robust self-triggered MPC with adaptive prediction horizon for perturbed nonlinear systems, *IEEE Transactions on Automatic Control*, 64 (11) (2019) 4780-4787.

[24] L. Dai, M. Cannon, F. Yang and S. Yan, Fast self-triggered MPC for constrained linear systems with additive disturbances, *IEEE Transactions on Automatic Control*, 66 (8) (2021) 3624-3637.

[25] L. Lu and J. M. Maciejowski, Self-triggered MPC with performance guarantee using relaxed dynamic programming, *Automatica*, 114 (2020) 108803.

[26] L. Lu, D. Limon and I. Kolmanovsky, Self-triggered MPC with performance guarantee for tracking piecewise constant reference signals, *Automatica*, 142 (2022) 110364.

[27] Y. Yao, X. Chen, H. Li and G. Li, Suspension parameters

design for robust and adaptive lateral stability of high-speed train, *Vehicle System Dynamics*, 61 (4) (2023) 943-967.
[28] W. Zhai, V*ehicle-Track Coupled Dynamics*, China Railway Press, Beijing, China (2015).
[29] W. Chen, D. J. Ballance, P. J. Gawthrop and J. O'Reilly, A nonlinear disturbance observer for robotic manipulators, *IEEE Transactions on Industrial Electronics*, 47 (4) (2000) 932-938.
[30] Y. Danayiyen, K. Lee, M. Choi and Y. I. lee, Model predictive control of uninterruptible power supply with robust disturbance observer, *Energies*, 12 (15) (2019) 2871.
[31] N. N. Nam, N.-D. Nguyen, C. Yoon and Y. I. Lee, Disturbance observer-based robust model predictive control for a voltage sensorless grid-connected inverter with an LCL filter, *IEEE Access*, 9 (2021) 109793.
[32] X. Li, Q. Yang, W. Tian, P. Karamanakos and R. Kennel, A dual reference frame multistep direct model predictive current control with a disturbance observer for SPMSM drives, *IEEE Transactions on Power Electronics*, 37 (3) (2021) 2857-2869.
[33] J. Yang, W. Zheng, S. Li, B. Wu and M. Cheng, Design of a prediction accuracy enhanced continuous-time MPC for disturbed systems via a disturbance observer, *IEEE Transactions on Industrial Electronics*, 62 (9) (2015) 5807-5816.
[34] GB/T 5599-2019, *Specification for Dynamic Performance Assessment and Testing Verification of Rolling Stock*, China National Bureau of Standards, China (2019).
[35] W. Zhang, R. Luo, C. Song and J. Fan, Hunting control of high speed train using traction motor as dynamic absorber, *Journal of Traffic and Transportation Engineering*, 20 (5) (2021) 125-134.
[36] P. Wang, S. Wang, D. Yang and D. Si, Study on adaptability of high-speed turnout under condition of designed speed, *Journal of the China Railway Society*, 44 (6) (2022) 75-83.
[37] A. Yang, F. Yang, J. Sun, H. Diao, J. Xu, H. Li and W. Chang, Study on dynamic management limit of geometric irregularities in turnout area of high speed railway, *Railway Engineering*, 62 (10) (2022) 35-39.
[38] D. Wang, C. Chen and S. Xiong, Lateral stability fuzzy control of high-speed train under aerodynamic load, *Machinery Design & Manufacture* (12) (2020) 87-90.

Ruqiang Mou received his M.A. degree in Mechatronic Engineering from Sichuan University in 2016, where he is currently pursuing the Ph.D. degree in Mechatronic Engineering from Southwest Jiaotong University, Chengdu, China. He is a lecturer of the Department of Automation Engineering, The Engineering & Technical College of Chengdu University of Technology. His research interests include robot mechanism and control, vehicle system dynamics and vibration control, mechatronics design.

Chunjun Chen received the Ph.D. degree from Southwest Jiaotong University in 2006 and the M.A. degree from University of Electronic Science and Technology of China in 1993. He is a Professor of School of Mechanical Engineering, Southwest Jiaotong University, Director of Department of Measure-ment and Control and Mechano-electronic Measurement and Control Laboratorial Center and Deputy Director of the Technology and Equipment of Rail Transit Operation and Maintenance Key Laboratory of Sichuan Province. His research interests include vibration, noise and aerodynamics of high-speed trains, traffic equipment, electromechanical systems, advanced control and measurement theory, electromechanical control and measurement system.

Chaoyue Chen is currently pursuing the Ph.D. degree in Mechatronic Engineering from Southwest Jiaotong University, Chengdu, China. His research interests include vehicle system dynamics, mechanical system dynamics and advanced control strategy.

Yaowen Zhang received the B.S. degree in mechanical engineering from Southwest Jiaotong University, Chengdu, China, in 2020, where he is currently pursuing the Ph.D. degree in Mechatronic Engineering from Southwest Jiaotong University. His current research interests include semi-active control and vehicle system dynamics.